Nanoscale

Composition-Induced Type I and Direct Bandgap Transition Metal Dichalcogenides Alloy Vertical Heterojunctions

Journal:	*Nanoscale*
Manuscript ID	NR-ART-09-2019-008345.R1
Article Type:	Paper
Date Submitted by the Author:	11-Nov-2019
Complete List of Authors:	Zhou, Songsong; University of Pennsylvania, Materials Science and Engineering Ning, Jinliang; Tulane University, Department of Physics and Engineering Physics Sun, Jianwei; Tulane University, Physics Srolovitz, David ; City University of Hong Kong, Materials Science and Engineering

Journal Name

ARTICLE TYPE

Cite this: DOI: 00.0000/xxxxxxxxxx

Composition-Induced Type I and Direct Bandgap Transition Metal Dichalcogenides Alloy Vertical Heterojunctions

Songsong Zhou,[a] Jinliang Ning,[b] Jianwei Sun,[b] and David J. Srolovitz*[a,c,d]

Received Date
Accepted Date

DOI: 00.0000/xxxxxxxxxx

While members of the 2D semiconducting transition metal dichalcogenide (TMD) family MX_2 (M={Mo,W}, X={S,Se}) are promising for device applications, stacked layer (vertical) heterojunctions exhibit features that make them inappropriate for light-emitting applications. Such vertical heterojunctions exhibit Type II, rather than the preferred Type I band alignment. Using density functional theory calculations, we identify the pseudo-binary and quaternary alloy composition range for which band alignment is Type I. While broad regions of composition space lead to Type I band alignment, most light-emitting devices require direct bandgaps. We demonstrate that by taking advantage of alloying and/or twisting between layers, a wide range of Type I, direct bandgap stacked layer (vertical) heterojunctions are achievable. These results and the underlying method developed here provide new opportunities for TMD vertical heterojunction device optimization and opens the door to new classes of TMD vertical heterojunction device applications.

1 Introduction

Heterojunctions, interfaces separating two dissimilar semiconducting materials, are the fundamental building blocks of microelectronic and optoelectronic devices, including solar cells, transistors, and light-emitting diodes[1–4]. The distinct electronic properties of the two materials result in discontinuities in the band structure at the junction (relaxed via charge flow across the junction). This band discontinuity/band alignment determines, to a large extent, the electronic behavior of the heterojunction. Heterojunctions are classified into three types based upon the relative valence band maximum (VBM) and conduction band minimum (CBM) in the two semiconductors. Type I heterojunctions are characterized by the bandgap of one semiconductor lying entirely within the bandgap of the other (see Fig. 1c). Here, both holes and electrons are confined in the semiconductor with the smaller bandgap; this is ideal for maximizing the emission efficiency of light-emitting devices[4,5]. Type II heterojunctions are characterized by partial overlap of the bandgaps of the two semiconductors (see Figs.1b,d); in this case, electrons and holes preferentially populate the semiconductors on opposites sides of the heterojunction. This is ideal for applications that depend on carrier separation, such as solar cells[6,7].

The emergence of two-dimensional (2D) materials with unique electronic properties provides opportunities for both new classes of devices and devices with superior performance[8–10]. 2D semiconducting transitional metal dichalcogenide (TMD) have received considerable recent attention because of their distinct electronic properties appropriate for a wide-range of device applications[9,11–15]. In these applications, vertical TMD heterojunctions (i.e., a van der Waals bonded stack of dissimilar TMD monolayers) are widely used[8,16].

In the present work, we focus on the most common family of TMDs; i.e., MX_2, where M={Mo,W}, X={S,Se}. Both experimental observations and first-principle calculations suggest that vertical heterojunctions in this TMD family are all Type II[17–23]. Creating Type I TMD vertical heterojunctions in this family remains an outstanding challenge. One possible approach to obtaining stacked TMD heterojunctions of different types is through transition metals (M) and/or chalcogens (X) substitution. Here, we suggest an alloying route to achieving both Type I and II vertical heterojunctions within this single family of TMDs. Recently, TMD alloys (e.g., $Mo_{(1-x)}W_xS_2$ or $MoS_{2(1-x)}Se_{2x}$) have attracted broad interest[24–30], largely because alloying provides a means of continuously tuning the TMD bandgap[25,28–32]. Manipulation of the composition of the two TMDs in a vertical heterostructure may provide routes to achieving both types of heterojunctions with

[a] Department of Materials Science and Engineering, University of Pennsylvania, Philadelphia, Pennsylvania 19104, USA, E-mail: srol@seas.upenn.edu
[b] Department of Physics and Engineering Physics, Tulane University, New Orleans, Louisiana, 70118, USA
[c] Department of Mechanical Engineering and Applied Mechanics, University of Pennsylvania, Philadelphia, Pennsylvania 19104, US
[d] Department of Materials Science and Engineering, City University of Hong Kong, Hong Kong SAR

† Electronic Supplementary Information (ESI) available: [details of any supplementary information available should be included here]. See DOI: 00.0000/00000000.

tunable band structures for particular applications (e.g., varying composition to manipulate light emission spectra). These TMD alloy heterojunctions may be fabricated by mechanically stacking two alloy monolayers. This method generally introduces some interlayer rotation. It should also be possible to synthesis alloy heterojunction by direct growth of the bilayer using CVD. Type II lateral TMD alloy heterojunctions have been experimentally realized[33]. In the present work, we employ *ab initio* density functional theory (DFT) methods to investigate how to manipulate band alignment in vertical heterojunctions to induce a Type I/II transitions. Further, we demonstate that the required direct bandgap for Type I heterojunction can be achieved by taking advantage of alloying and/or twisting between layers.

2 Results and discussion

2.1 Anderson's rule band alignment

Consider two Type II heterojunctions consisting of pure compounds, A/C and B/C, where A and B can be continuously alloyed to form $A_xB_{(1-x)}$. If the compound A in the A/C heterojunction has a CBM and VBM lower than those of C, and the B/C heterojunction has B with a CBM and VBM higher than those in C, the band edges must cross at some composition $A_xB_{(1-x)}/C$ $(0 < x < 1)$. This is shown schematically in Fig. 1, where we explicitly assumed that the alloy CBM and VBM vary monotonically with composition, x. The CBMs and VBMs of $A_xB_{(1-x)}$ and C cross at $x = x_1$ and x_2, respectively (in general $x_1 \neq x_2$). In this schematic, the heterojunction is Type I for $x_1 < x < x_2$ and Type II otherwise. If, on the other hand, the CBM and VBM do not vary monotonically with composition, multiple crossover points may occur such that Type I heterojunctions may be formed in multiple distinct composition ranges. Nonetheless, if there is a crossover in the CBM and VBM between the pure compounds, Type I/II transition(s) in the TMD alloy heterojunctions must occur.

The standard approach to validate this concept would be to calculate the heterojunction band structure as a function of alloy semiconductor composition. However, this approach is not practical here for two reasons. First, in most TMD heterojunctions, the lattice constants of the two constituent monolayers are different (the TMD monolayer lattice constant depends on the chalcogenide species). For example, while the pure TMD monolayers MoS_2 and WS_2 have nearly same lattice constant, $MoSe_2$ and WSe_2 have lattice constant which are 4.4% larger. For the alloy monolayers, the lattice constant is approximately linear in the chalcogenide species concentrations. Given the weak van der Waals bonding between the vertically stacked TMD monolayers, the heterojunctions will be formed by two lattice-mismatched monolayers (i.e., no heteroepitaxy). The misfit may be relaxed in free-standing bilayers by sheet curvature, by the introduction of an array of interlayer dislocations (with edge character) between the sheets, and/or by rotation of the sheets relative to one another (creating a Moiré pattern)[34–37]. Simulating such structures requires too large of a supercell for systematic, accurate DFT calculations. Moreover, unlike in the case of pure TMD heterojunctions (for which relatively small primitive cell building blocks may be used), the simulation of solid solution alloys requires much larger

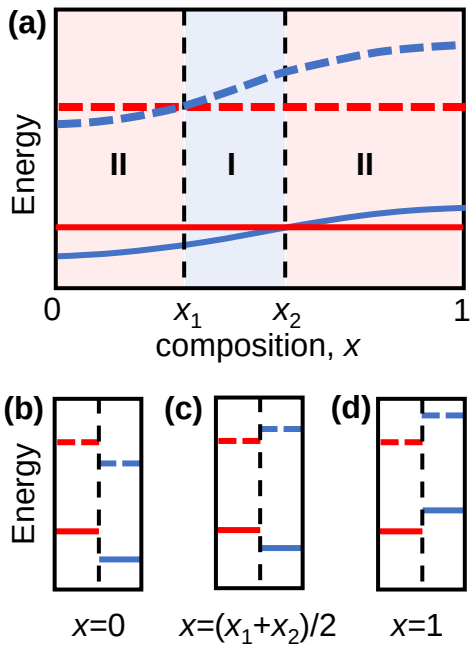

Fig. 1 (a) Schematic plot of the conduction band minimum (CBM, dotted blue) and valence band maximum VBM (solid blue) in an $A_{(1-x)}B_x$ alloy (blue lines) as a function of composition x and for a compound C (independent of x, red lines) that are joined to form a heterojunction. For $x_1 < x < x_2$ the heterojunction is of Type I (i.e., the bandgap of C lies completely within the bandgap of the $A_{(1-x)}B_x$ alloy), while for $0 < x < x_1$ and $x_2 < x < 1$ the heterojunction of Type II (i.e., the bandgaps of compound C and the $A_{(1-x)}B_x$ alloy only partially overlap) - as illustrated in extremis in (b)-(d).

supercells. For these reasons, direct DFT calculation of such long period (for small misfit), random alloy structures is not practical.

To circumvent this problem, we calculated the CBM and VBM of the individual (unstrained) alloy monolayers to determine the heterojunction band alignment. To verify the validity of this approach, we examine the case of pure TMD monolayer heterojunctions (MoS_2 / WS_2) before applying it to alloy heterojunctions. If there is no interaction between the two monolayers, the band structure of the heterojunction would simply be the superposition of those of the two monolayers. In this case, band alignment may simply be determined by aligning the bands of the two alloys with respect to the vacuum level, as per Anderson's rule[38]. However, there is always some interaction between monolayers.

In our TMD case, the monolayers have direct bandgaps located at the high symmetry point K; there is an additional (local) maximum in the VBM at Γ that is only slightly lower than that at K. When the MoS_2 / WS_2 heterojunction is formed, the band structure changes are as shown in Fig. 2 (a). Here, we focus on the VBMs at K and Γ and the CBM at K. The VBM at Γ in the heterojunctions increase significantly relative to the VBM of each monolayer. However, the VBM/CBM at K remains the same as in the individual monolayers. The increasing in VBM at Γ is attributable to interlayer interactions. As shown in Fig. 2 (b), this is because the orbital contributed to the VBM at Γ is directed normal to the monolayers. The VBM at Γ shows strong orbital mixing from the two monolayers; this increases the VBM at Γ. However,

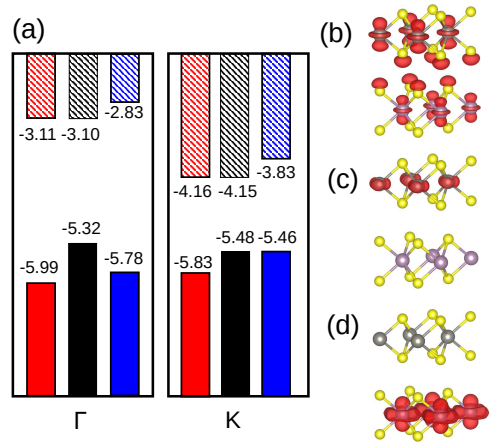

Fig. 2 (a) Schematic plot of the conduction band minimum (CBM, diagonal stripes) and valence band maximum (VBM, solid shading) at the Γ (left) and K (right) points, for MoS_2 (red) and WS_2 (blue) monolayers and their heterojunction (black), respectively. All the energy level are aligned respect to vacuum level. (b)(c)(d) Partial charge density in the WS_2/MoS_2 heterojunction corresponding to the VBM at Γ, VBM at K and CBM at K, respectively. The purple, grey and yellow circles represent the Mo, W and S atom, respectively. Note the orbitals directed normal to both monolayers only in (b).

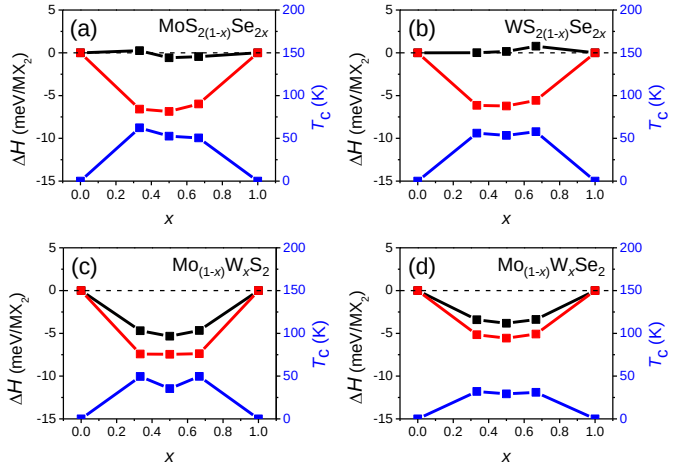

Fig. 3 The alloy formation enthalpy and the ordered/disordered transition temperature T_c for (a) $MoS_{2(1-x)}Se_{2x}$, (b) $WS_{2(1-x)}Se_{2x}$, (c) $Mo_{(1-x)}W_xS_2$ and (d) $Mo_{(1-x)}W_xSe_2$ alloys. The red and black curves correspond to the formation enthalpies of the ordered and disordered alloys, respectively and the blue curve shows $T_c(x)$.

at the VBMs and CBMs at K, the orbitals are localized within the plane and thus cause little interlayer interaction (see Fig. 2 (c-d)); hence the VBMs and CBMs at K remain nearly unchanged when the two monolayers are joined to form a heterojunctions. In other word, Anderson's rule is applicable at K and can be used to measure band alignment. This approach has been verified experimentally[39]. However, since the VBM at Γ may be higher than that at K in the heterojunction, this may lead to an indirect bandgap. This is undesirable for Type I heterojunction applications. Therefore, two questions arise: (1) how does the CBM/VBM at K and the band alignment change with respect to alloy composition and (2) in what composition range that the Type I heterojunction has a direct bandgap.

In the following, we solve the first problem using the monolayer approach; i.e. we perform DFT calculations to determine the CBM/VBM for pesudo-binary and quaternary monolayer TMD alloys and corresponding band alignment . Then, we show that with considering rotating the two monolayers with respect to one another, the Type I heterojunctions may have direct bandgap.

2.2 Alloy monolayer structure

Before calculating the VBM and CBM of the alloy monolayers, we first determine their structures. Alloys may exist as disordered, ordered or phase-separated structures (as $T \to 0$ the only possibilities are ordering and phase separation); clearly, the electronic structure is sensitive to these structural differences. In pseudo-binary alloys, the ($T = 0$) ground states are known to be ordered[32,40,41]. We determined the ordered ground states using the cluster expansion (CE) approach[42], while the alloy configurations in the (finite-temperature) disordered state were modeled using special quasirandom structures (SQS)[43,44]. See the method section and supplementary information for more details.

Fig. 3 shows the formation enthalpy of the alloy ΔH as a function of composition for both the ordered and disordered alloys. In all cases, the ordered ground state has a lower enthalpy than the disordered state by less than 7 meV per MX_2. It is interesting to note that ΔH is nearly independent of the anion content but varies strongly with cation substitution in the disordered alloy. This may be attributed to local elastic distortions; the lattice constants of the mixed anion alloys are nearly linear in composition x, while the lattice constants of the mixed cation alloys are nearly independent of composition. While the configurational entropy of the classical ordered alloy is zero, the configuration entropy of a disordered alloy (per MX_2) may be estimated as $S \approx -Ak_B(x\ln x+(1-x)\ln(1-x))$, where $A = 1$ and 2 for the mixed cation and anion disordered alloys, respectively. We determine the order/disorder transition temperature $T_c(x)$ based on these enthalpies and configurational entropies, as shown in Fig. 3. The ordered/disordered transition temperature for all four alloy systems is less than 65 K, which is much lower than typical device operating and synthesis temperatures (600-900°C)[29,45]. This implies that the structures of the individual TMD alloy monolayers of interest should be disordered; hence, we focus on (SQS) disordered alloys.

2.3 Alloy heterojunction band alignment

We start from the band edge alignment of heterojunction composed of pesudo-binary alloys. Previous calculations for pure TMD compounds and alloys[32,40,46] use generalized gradient approximation and the Perdew-Burke-Ernzerhof (PBE) functionals[47]. However, local density and generalized gradient approximations yield unreliable bandgap predictions[48,49]. So these PBE results imply that the band alignment in $MoSe_2/WS_2$ heterojunctions is Type I[32,46], while experimental observations imply Type II[22,23,50]. To provide more accurate results, here we employ the

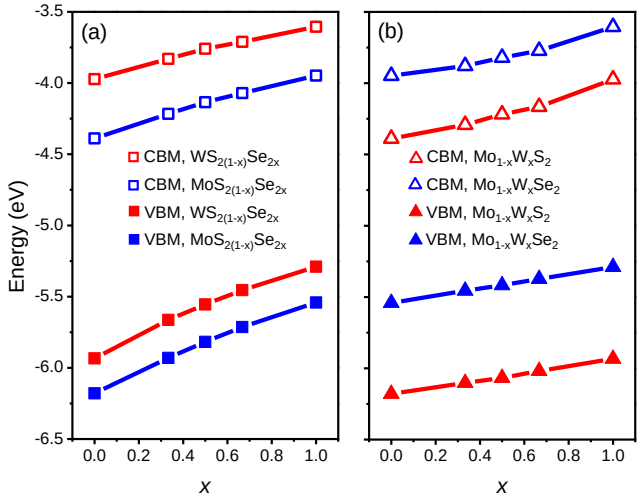

Fig. 4 The CBM and VBM as a function of composition x for the mixed (a) anion and (b) cation alloys, respectively (zero energy is the vacuum level).

Strongly Constrained and Appropriately Normed semilocal density functional (SCAN)[51] to calculate the CBM and VBM. This functional leads to more accurate predictions of the properties of many materials as compared with many other current functionals[52]. The results are shown in Fig. 4. Here, the $MoSe_2/WS_2$ heterojunction is Type II with the CBM of WS_2 ~25 meV lower than that of $MoSe_2$, in agreement with experiment[50]. Consistent with our assumption above, we find that the CBM and VBM vary monotonically with respect to composition x in all of the alloy systems. The CBM and VBM are well described by a second order polynomial $E(x) = E(1)x + E(0)(1-x) + wx(1-x)$, where $E(x)$ denotes the band edge energy (CBM or VBM) as a function of composition x, $E(0)$ and $E(1)$ are the band edge energies of the pure TMD compounds, and w is a parameter fit to the DFT data.

We determine the heterojunction band alignment from the band edge data for all six heterojunctions of two different TMD pseudo-binary alloy monolayers. While it is possible to fabricate heterojunctions where each side is from the same TMD pseudo-binary alloy system with different compositions (e.g. $Mo_{0.3}W_{0.7}S_2$ / $Mo_{0.5}W_{0.5}S_2$), we do not consider such junctions since they are inevitably Type II (both the VBM and CBM have the same monotonicity with respect to composition - see Fig. 4). The band alignment type and the effective bandgap (difference between the lowest CBM and highest VBM of the two monolayers) as a function of composition are shown in Fig. 5 for all six TMD pseudo-binary alloy heterojunctions. Among these, only three pseudo-binary alloy pairs exhibit both Type I and Type II heterojunctions; these are $MoS_{2(1-y)}Se_{2y}$ / $WS_{2(1-x)}Se_{2x}$, $WS_{2(1-y)}Se_{2y}$ / $Mo_{(1-x)}W_xSe_2$ and $MoS_{2(1-y)}Se_{2y}$ / $Mo_{(1-x)}W_xS_2$; the others yield only Type II heterojunctions.

The Type I/Type II transition in $MoS_{2(1-y)}Se_{2y}$ / $WS_{2(1-x)}Se_{2x}$ heterostructures can be easily understood. The $MoSe_2$ / $WS_{2(1-x)}Se_{2x}$ (along the $y = 1$ axis) heterojunction corresponds to the case shown in Fig. 1(a), as does the $MoS_{2(1-y)}Se_{2y}/WS_2$ (along the $x = 0$ axis) heterojunction. The Type I region is near

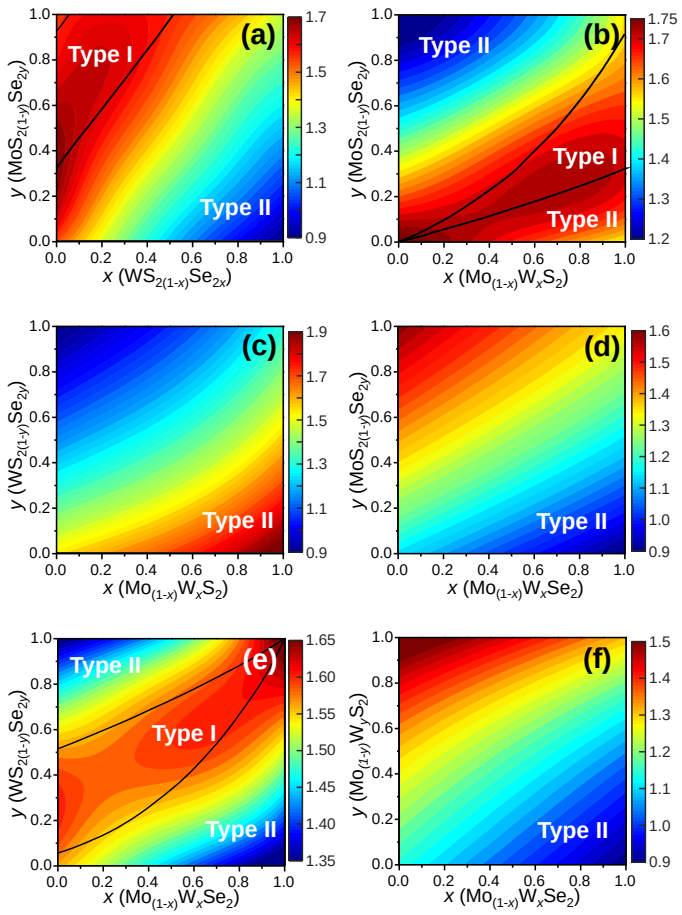

Fig. 5 The pseudo-binary heterojunction type diagrams for all six possible pseudo-binary alloy heterojunctions. The contours show the effective bandgap as a function of composition (fit to 25 compositions each). The black curves indicate the Type I/II transition boundaries, corresponding to the zero contour lines of the CBM difference or VBM difference.

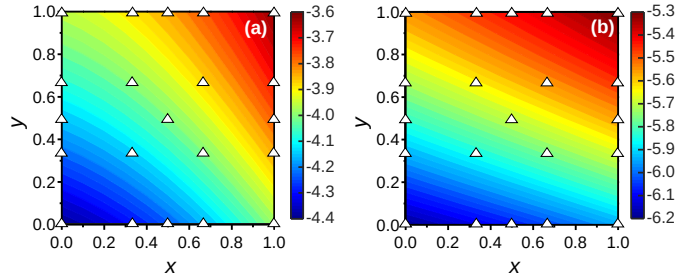

Fig. 6 Contour plots of the (a) CBM and (b) VBM of quaternary alloy $Mo_{(1-x)}W_xS_{2(1-y)}Se_{2y}$ monolayers based on the *ab initio* data at the compositions indicated by the open triangles.

Table 1 The parameters $P_{i,j}$ (eV) in Eq. (1) for the CBM and VBM for the quaternary {MoW}{SeS}$_2$ alloy for $N = 1$ and 2. The root-mean-square errors (RMSE) in the CBM and VBM from fitting $P_{i,j}$ to the first principles data.

	N	P_{00}	P_{01}	P_{10}	P_{11}	P_{02}	P_{20}	P_{12}	P_{21}	P_{22}	RMSE
CBM	1	-4.3940	0.4342	0.4084	-0.0679						0.0321
VBM		-6.1630	0.6434	0.2561	0.0018						0.0269
CBM	2	-4.3860	0.5536	0.2262	-0.0938	-0.1162	0.1842	0.0027	0.0113	0.0118	0.0118
VBM		-6.1800	0.8124	0.2191	0.1151	-0.1726	0.0288	-0.0862	-0.0532	0.0261	0.0029

the top left corner of Fig. 5(a) because the CBM difference between $MoSe_2$ and WS_2 is relatively small. This implies that relatively small anion doping into WS_2 or $MoSe_2$ can convert the $MoSe_2$/WS_2 heterojunction to Type I.

Like in the $MoS_{2(1-y)}Se_{2y}$ / $WS_{2(1-x)}Se_{2x}$ pseudo-binary heterojunction case, we also find a transition in heterojunction type for $MoS_{2(1-y)}Se_{2y}$ / $Mo_{(1-x)}W_xS_2$. Such a transition is not surprising in light of the fact that the CBM (VBM) for MoS_2 is below that for WS_2 and $MoSe_2$ is above that for WS_2; this implies that at some composition $\{x_1, y_1\}$ ($\{x_2, y_2\}$) the CBM (VBM) difference between these two alloys must be zero. Examination of Fig. 5(b) shows that there are compositions y for which heterojunction are Type I over the entire composition range x. Similarly, there are compositions x for which heterojunction are Type I over nearly) the entire composition range y. Note that the Type I composition range shrinks to zero at the bottom left corner of Fig. 5(b), as it must since $(x = 0, y = 0)$ the vertical heterojunction is simply a homogeneous MoS_2 bilayer (i.e., a homo- rather than hetero-junction). A similar argument pertains to the $WS_{2(1-y)}Se_{2y}$/$Mo_{(1-x)}W_xSe_2$ pseudo-binary vertical heterojunction case (Fig. 5(e)) except that in this case it is the $(x = 1, y = 1)$ limit that the heterojunction is actually a WSe_2 bilayer.

In addition to modifying the heterojunction from Type II to Type I by manipulating the compositions in the {MoW}{SeS}$_2$ TMD pseudo-binary alloy system, changing composition also presents opportunities to tune the CBM (VBM) difference and effective bandgap of the heterojunction (which, for example, gives control of the light emission wavelength in Type I heterojunctions). The effective bandgap of TMD pseudo-binary alloy heterojunctions are shown as the contours in Fig. 5 as a function of alloy composition $\{x, y\}$. The Type I heterojunctions exhibit effective bandgaps in the $1.6 - 1.8$ eV range; while the effective range of Type II heterojunction bandgaps can be tuned over a much great range $0.9 - 2.0$ eV. The variations of the CBM and VBM across the entire range of TMD monolayer compositions are reported in the supplementary information.

2.4 Quaternary alloys

Now we further extend our result to quaternary alloys ($Mo_{(1-x)}W_xS_{2(1-y)}Se_{2y}$) and their heterojunctions. Such a quaternary TMD was recently synthesized via chemical vapor deposition[30]. Compared to the pseudo-binary alloys, varying both x and y in a quaternary alloy provides greater flexibility for tuning the bandgap and band offsets to obtain Type I TMD heterojunctions (such quaternary systems may also lead to lower synthesis temperatures[30]).

We first calculated the CBM and VBM of the quaternary $Mo_{(1-x)}W_xS_{2(1-y)}Se_{2y}$ TMD alloy monolayers as a function of x and y (see Fig. 6), where the alloy structures were represented using the SQS approach. In addition to the data points obtained for the pseudo-binary alloys (present along the axes in Fig. 6), we add five quaternary alloy data points at a small set of additional (x, y) pairs (21 data points in total). Because the CBM and VBM are smooth, monotonic functions of x and y, they are well fit by a low order N polynomial

$$E(x,y) = \sum_{i=0}^{N}\sum_{j=0}^{N} P_{i,j}x^i y^j, \quad (1)$$

where $E(x,y)$ is either the CBM or VBM, x and y are the W and Se compositions, respectively and $P_{i,j}$ are fitting parameters. The values of the $P_{i,j}$ are shown in Table 1 for $N = 1$ and 2. Examination of the fitting errors indicate that both the CBM and VBM are well-described by Eq. (1), truncated at low order ($N = 1$ and 2).

Compared to that of the pseudo-binary alloys, the quaternary system exhibits larger ranges of both the CBM (-3.6 to -4.4 eV) and VBM (-5.3 to -6.2 eV). Unfortunately, such band alignment diagrams are 4-dimensional and not easily visualized. However, the alignment and gap value can be easily determined by using above band edge data. The heterojunction is of Type I if $(\Delta E^{\mathrm{CBM}})(\Delta E^{\mathrm{VBM}}) < 0$ (or Type II otherwise), where ΔE^{CBM} and ΔE^{VBM} are the CBM and VBM difference, respectively (see Eq. 1).

2.5 Direct vs indirect bandgaps: twisted bilayers

To this point, we focused largely on the determination of band edge alignment at the K point. However, it is unclear in what (if any) composition ranges the proposed Type I heterojunctions have direct bandgaps. In these Type I TMD alloy heterojunctions, the bandgap is direct when the VBM at K is higher than the VBM at Γ (recall that the VBM at K is independent of interlayer interaction and is only a function of composition x). The VBM at Γ is determined by interlayer interactions, which may be affected by rotation of one monolayer with respect to the other (about the monolayer normal). Monolayer rotation disrupts the alignment of orbitals directed normal to the interface (this is relevant to the VBM at Γ); rotation effectively decouples monolayers and weakens interlayer interactions, as reported for bilayer graphene. In MoS_2/WS_2, the two monolayers have no lattice mismatch; the heterojunction has coherent AA′ stacking (where the transition metal in one monolayer lies directly above the chalcogenide atoms in the other monolayer). In this case, the interlayer interactions are strong and heterojunction has indirect bandgap. However, when the layers are rotated with respect to one another, the coherent AA′ stacking is replaced by an incoherent (or irrational) stacking except at a countable set of rotation angles. This irra-

tional stacking decouples the two monolayers and weakens the interlayer interaction at Γ. Rotations between monolayers in vertical heterojunction are very common as a result of heterojunction production methods (fabrication by mechanical exfoliation and bonding commonly results in monolayer rotations). Layer rotation may even be present based on energetic considerations (e.g., rotated epitaxy to accommodate misfit when two monolayers have different lattice constants). So generally, the VBM at Γ is a function of both composition and rotation.

We investigate the dependence of the VBM at Γ on rotation using a supercell of sufficient size to accommodate the twisted bilayer. We focus first on heterojunctions of pure TMD heterojunctions in order to validate our approach and then apply it to TMD alloy heterojunctions. In particular, we first investigate the lattice-matched case for a MoS_2/WS_2 heterojunction example. The two layers are rotated with respect to one another by a rotation angle, θ, the angle between armchair directions in the two monolayers (θ=0 corresponds to the coherent AA′ stacking). Since the two layers are rotated relative to one another, we account for supercell band folding in the evaluation of the VBM at Γ and K using an effective band structure approach[53]. The states are first projected from the heterojunction onto each monolayer and unfolded relative to the primitive cell of each monolayer.

The VBM for the MoS_2/WS_2 heterojunction at the Γ and K points is shown in Fig. 7 (a) for several rotation angles. These angles are chosen such that the rotated heterojunction supercell has small lattice misfit ($\leq 0.5\%$) between two monolayers and the supercell sufficiently small for (reasonable) DFT calculations. The VBM at K is nearly rotation angle independent at a value close to that of a WS_2 monolayer at K; this further validates the Anderson's rule approach at K. While the VBM at Γ is higher than that at K at θ=0, the VBM at Γ changes significantly with respect to θ near θ= 0 and 60°, but nearly constant at intermediate rotation angles. In this intermediate angle range, the VBM at Γ is still higher than that at K, but the difference is significantly smaller than that at θ=0 (0.03 vs. 0.16 eV). However, increasing θ beyond some critical angle, the VBM at Γ drops below that at K. The lowest VBM at Γ (-5.56 eV) is 0.22 eV higher than that in WS_2 (-5.78 eV). This is because that, despite being weakened by rotation, interaction between layers still exists for the VBM at Γ. We note that lattice-matched monoloyers are rare in the entire composition space (along a small set of curves in the two-dimensional bilayer pseudo-binary composition space). For example, lattice-matching in $MoS_{2(1-y)}Se_{2y}/WS_{2(1-x)}Se_{2x}$ occurs along $y \approx x$ (Fig. 5 (a)).

As an example of a more common lattice-mismatched case, we examine MoS_2/WSe_2 heterojunctions (see Fig. 7 (b)). Note that because the two monolayers have different lattice constants, θ=0 does not correspond to a coherent structure as in the lattice-matched case (there is no θ=0 data point in the figure since there requires a very large DFT supercell). As in the lattice-matched case, the VBM at K is nearly independent of rotation angle (-4.88 eV). For the three rotation angles examined here, the VBM at Γ is nearly independent of rotation angle and is consistently ~ 0.3 eV lower than that at K; i.e., the VBM is at K for all θ. This independence of the VBM at Γ on θ may be attributed to the fact that

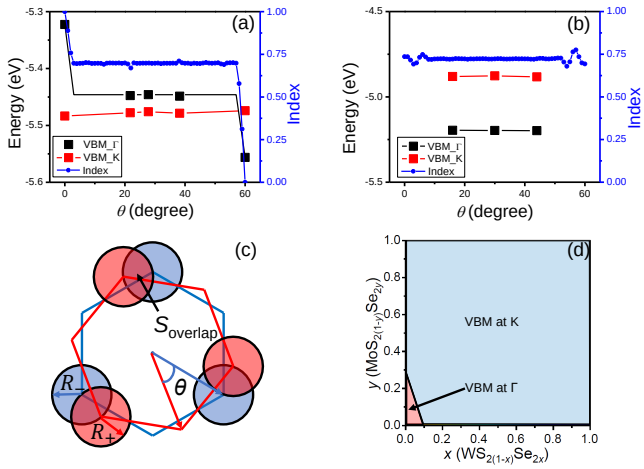

Fig. 7 The VBM at Γ (black) and K (red) for (a) lattice-matched MoS_2/WS_2 heterojunctions and (b) lattice-mismatched MoS_2/WSe_2 heterojunctions as a function of rotation angle θ, All the energy levels are aligned with respect to the vacuum level. An index (blue) is defined to measure the interlayer interaction strength as well as VBM at Γ. (c), schematic representation of geometric model: the red and blue circles of radius R_+ and R_- represent circles placed on calcogenide atoms in top and bottom monolayer, respectively. The rotation angle θ is defined as zero when there is minimum overlaping area in lattice-matched case, where the structure is coherent AA' stacking. (d), the composition regions of global VBM at K (cyan) and Γ (pink) in $MoS_{2(1-y)}Se_{2y}/WS_{2(1-x)}Se_{2x}$ alloy heterojunction of about 30° rotation. The composition region obtained by fitting the band edge data from four pure TMD heterojunctions (corners) (30° rotation for lattice-mismatched cases and 28° rotation for lattice-matched cases).

the lattice-mismatch between the layers insures that the two layers will be incoherent (all incoherent cases have similar interlayer interaction strength). Any coherency will occur at a countable set of rotation angles and in very large periodic cells.

As our data in Fig. 7 are sparse, we further examine the effect of rotation on the basis of a simple geometric model to account for interlayer interactions on the VBM at Γ. Since the interlayer interactions are dominated by chalcogenide atom orbitals directed normal to the monolayer. We place circles of radius R_+ and R_- at the location of each chalcogen in the top and bottom monolayer, respectively, to crudely represent the lateral extent of the orbitals (Fig. 7c). We then examine the overlap (area) between the circles as a measure of the interlayer interaction strength. We define the interlayer interaction function as $I(\theta) = 1 - \frac{S_{overlap}(\theta)}{S_{total}}$, where $S_{overlap}(\theta)$ is the overlap area between circles in two monolayers,and S_{total} is the total area of circles in top monolayer at fixed material parameters (lattice constant ratio a_-/a_+, circle radius ratio R_-/R_+ and lattice constant to radius ratio R_+/a_+). In our examples, we set $R_+/a_+ = 1/2\sqrt{3}$ and $R_-/R_+ = 1$ and $a_-/a_+ = 1$ or 1.044 for lattice-matched and -mismatched cases, respectively. In the lattice-matched case (Fig. 7a), $I(\theta = 0)$=1 and drops abruptly to $I = 0.7$, remains nearly θ-independent until $\theta \approx 60°$ where it drops to $\theta(60°) = 0$. For the lattice-mismatched case, $I(\theta)$ is independent of θ over the entire angle range (apart from small variations near 0 and 60°). These trends are consis-

tent with our DFT data calculations for the VBM at Γ (Fig. 7a,b). This confirms the conclusion that the VBM at Γ is nearly independent of rotation angle and misfit for all TMD bilayers, except for a small set of special cases (e.g., lattice-matched case at $\theta = 0$). Note, since this index reflects bilayer registry, it also is an indicator of the relative energy of the different configurations (configurations of larger index have lower energy). These results imply that lattice-mismatched heterojunctions with different rotations have similar energy and are nearly equally stable.

We now consider the question of which alloy bilayer heterojunctions have direct bandgaps based on the assumption that the two monolayers are rotated with respect to one another by an angle not too near $\theta = 0$ or 60°. As an example, we focus on the $MoS_{2(1-y)}Se_{2y}/WS_{2(1-x)}Se_{2x}$ alloy heterojunction with about 30° rotation. We first calculate the band edge of pure TMD heterojunctions of about 30° rotation (30° for lattice-mismatched cases and 28° for lattice-matched cases). Then use these data to estimate the composition region (via a simple spline) where the global VBM located at Γ or K (Fig. 7d). Only the MoS_2/WS_2 heterojunction has a higher VBM at Γ than the VBM at K such that the composition region where the VBM at Γ is limited to near the bottom left corner of Fig. 7d. We also ensure that the CBM is located at K for all cases here ($WS_2/MoSe_2$ has degenerate global CBM states). As the Type I composition region is located near the top left corner of the diagram (Fig. 5a) for this alloy bilayer heterojunction, the overlap between these regions (Type I and global VBM at Γ) should be very limited. Hence, the Type I heterojunctions in this alloy system should exhibit direct bandgaps. In particular, in the $MoS_{2(1-y)}Se_{2y}/WS_{2(1-x)}Se_{2x}$ alloy heterojunction case, Type I direct bandgaps should be achievable in the following composition range $1.34x+0.33<y<1.17x+0.93$, independent of rotation angle (as long as the lattice parameter misfit is not 0.

Note that this direct bandgap only applies to Type I heterojunctions, where the global CBM and VBM are located in the same monolayer. In Type II heterojunctions (where the VBM and CBM at K belong to different monolayers), rotation implies that the K points in the two monolayers are not identical. Such rotated Type II heterojunctions will have an indirect bandgap even when the global VBM is located at K. Fortunately, most applications of Type II heterojunctions are not optical and, hence, direct bandgaps are unnecessary.

3 Conclusion

While bilayer, vertical heterojunctions of $\{Mo,W\}\{S,Se\}_2$ monolayers have been widely discussed for microelectronics and optoelectronic applications, all such binary monolayer heterojunctions are limited to Type II band alignment. We examined VBM and CBM band alignment in heterojunctions where each monolayer is from the $Mo_{(1-x)}W_xS_{2(1-y)}Se_{2y}$ quaternary alloy family. The VBM and CBM at the K point and the bandgap were shown to vary continuously with composition over the entire alloy space. The effective bandgap in these TMD alloy heterojunctions is tunable from 0.9 to 2.0 eV. We demonstrate that in half of the pseudo-binary cases, there are broad composition ranges for which Type I vertical TMD heterojunction band alignment occurs and provide a general framework to predict the heterojunction band alignment.

Direct bandgap Type I heterojunction are preferred for light-emitting applications. Indirect bandgaps may arise because of interactions between monolayers (not captured by Anderson's rule); orbital overlap between chalcogens on the two layers give rise to a VBM at the Γ (rather than K) point. On the other hand, the VBM at the K point is largely unaffected by joining the monolayers into a heterojunction. The degree of orbital overlap is strongly influenced by the relative rotation of one monolayer with respect to the other. Here we determined the band edges as a function of rotation angle for both lattice-matched and -mismatched bilayers, and provided a simple, predictive geometrical model to capture this effect. In the lattice-matched case, the VBM at Γ is independent of rotation angle except very near the special angles of 0 and 60°. In the lattice-mismatched case, the resultant incommensurability ensures that VBM at Γ is a constant. This is consistent with the weak van der Waals interactions between layers and the high in-plane monolayer stiffness that resists strained heteroepitaxy. Based on these conclusions and data, we predict that Type I alloy heterojunction of direct bandgap are achievable over a wide range of TMD composition and/or rotation space.

The present results provide alloying and/or monolayer rotation approach to creating direct bandgap, Type I TMD alloy-based heterojunctions. In particular, we provide alloy composition ranges in the pseudo-binary and quaternary $\{Mo,W\}\{S,Se\}_2$ system for which such direct, Type I heterojunctions should be achievable.

4 Methods

Density functional theory (DFT) calculations were performed using the Vienna *Ab Initio* Simulation Package (VASP)[54,55] using both a plane-wave basis set and the projector augmented wave method[56,57]. The Strongly Constrained and Appropriately Normed (SCAN) semilocal density functional was employed[51] with a $41 \times 41 \times 1$ Γ-centered k-point mesh (in the primitive cell) and an energy cutoff of 520 eV for band edge calculations. A vacuum layer of at least 20Å perpendicular to the monolayer was employed. Atomic structures were relaxed until the total force on each atom was ≤ 0.01 eV/Å.

The heterojunction data in Figs. 2 and 7, were obtained using the PBE functional with an energy cutoff of 500 eV. The Tkatchenko-Scheffler method was employed to describe the Van der Waals interaction between monolayers. For the supercells with rotation, because the two monolayer are twisted relative to each other in the rotated bilayer heterojunction, the calculated band structure is folded. To unfold the bands and extract the desired VBM states, we employed the BandUP code[58,59]. Here, the heterojunction supercell states are projected to the Brillouin zone of each of the monolayers and unfolded to retrieve the effective band structure[53] in their respective primitive cells. When projected to different monolayers, the k-points of the two monolayers (e.g., the high symmetry point K) are not identical except at the Γ point.

Both Special Quasirandom Structures[43,44] (SQS) and cluster expansion[42] approaches were employed, within the Alloy Theoretic Automated Toolkit (ATAT)[60]. For the SQS, we ensured

that the correlation function for the first-third nearest neighbor pair clusters is consistent with a perfectly random alloy, and minimized the correlation function difference (compared with the perfectly random alloy) of the two most compact triplet clusters (i.e., the first and second nearest triplet). For the pseudo-binary alloys at compositions x=1/3, 2/3 and 1/2, we used a $3\times3\sqrt{3}\times1$, $3\times3\sqrt{3}\times1$ and $4\times3\sqrt{3}\times1$ rectangular supercell, respectively. For the quaternary alloys, at composition (1/3, 1/3), (2/3, 1/3), (1/3, 2/3) and (2/3, 2/3), a $3\times3\sqrt{3}\times1$ rectangular supercell was used and for the composition (1/2, 1/2), a $4\times3\sqrt{3}\times1$ rectangular supercell was employed. For the cluster expansion and formation enthalpy calculations for the alloys, we employed the the Perdew-Burke-Ernzerhof functional (PBE)[47] with an energy cutoff of 350 eV.

Conflicts of interest

There are no conflicts to declare.

Acknowledgements

This work was supported in its entirety as part of the Center for the Computational Design of Functional Layered Materials, an Energy Frontier Research Center funded by the U.S. Department of Energy (DOE), Office of Science, Basic Energy Sciences(BES) under Award DE-SC0012575.

Notes and references

1 J. D. Werking, C. R. Bolognesi, L.-D. Chang, C. Nguyen, E. L. Hu and H. Kroemer, *IEEE Electron Device Letters*, 1992, **13**, 164–166.

2 A. Nourbakhsh, A. Zubair, M. S. Dresselhaus and T. Palacios, *Nano Letters*, 2016, **16**, 1359–1366.

3 D. Jariwala, A. R. Davoyan, J. Wong and H. A. Atwater, *ACS Photonics*, 2017, **4**, 2962–2970.

4 F. Withers, O. Del Pozo-Zamudio, A. Mishchenko, A. P. Rooney, A. Gholinia, K. Watanabe, T. Taniguchi, S. J. Haigh, A. K. Geim, A. I. Tartakovskii and K. S. Novoselov, *Nature Materials*, 2015, **14**, 301–306.

5 P. Waltereit, O. Brandt, A. Trampert, H. T. Grahn, J. Menniger, M. Ramsteiner, M. Reiche and K. H. Ploog, *Nature*, 2000, **406**, 865–868.

6 Y. J. Song, M. R. Park, E. Guliants and W. A. Anderson, *Solar Energy Materials and Solar Cells*, 2000, **64**, 225–240.

7 R. Cheng, D. Li, H. Zhou, C. Wang, A. Yin, S. Jiang, Y. Liu, Y. Chen, Y. Huang and X. Duan, *Nano Letters*, 2014, **14**, 5590–5597.

8 A. K. Geim and I. V. Grigorieva, *Nature*, 2013, **499**, 419–425.

9 Y. Gong, J. Lin, X. Wang, G. Shi, S. Lei, Z. Lin, X. Zou, G. Ye, R. Vajtai, B. I. Yakobson, H. Terrones, M. Terrones, B. K. Tay, J. Lou, S. T. Pantelides, Z. Liu, W. Zhou and P. M. Ajayan, *Nature Materials*, 2014, **13**, 1135–1142.

10 P. Rivera, K. L. Seyler, H. Yu, J. R. Schaibley, J. Yan, D. G. Mandrus, W. Yao and X. Xu, *Science*, 2016, **351**, 688–691.

11 K. F. Mak, C. Lee, J. Hone, J. Shan and T. F. Heinz, *Physical Review Letters*, 2010, **105**, 136805.

12 A. Splendiani, L. Sun, Y. Zhang, T. Li, J. Kim, C.-Y. Chim, G. Galli and F. Wang, *Nano Letters*, 2010, **10**, 1271–1275.

13 C. Huang, S. Wu, A. M. Sanchez, J. J. P. Peters, R. Beanland, J. S. Ross, P. Rivera, W. Yao, D. H. Cobden and X. Xu, *Nature Materials*, 2014, **13**, 1096–1101.

14 M.-Y. Li, Y. Shi, C.-C. Cheng, L.-S. Lu, Y.-C. Lin, H.-L. Tang, M.-L. Tsai, C.-W. Chu, K.-H. Wei, J.-H. He, W.-H. Chang, K. Suenaga and L.-J. Li, *Science*, 2015, **349**, 524–528.

15 F. M. Pesci, M. S. Sokolikova, C. Grotta, P. C. Sherrell, F. Reale, K. Sharda, N. Ni, P. Palczynski and C. Mattevi, *ACS Catalysis*, 2017, **7**, 4990–4998.

16 C.-H. Lee, G.-H. Lee, A. M. Van Der Zande, W. Chen, Y. Li, M. Han, X. Cui, G. Arefe, C. Nuckolls, T. F. Heinz, J. Guo, J. Hone and P. Kim, *Nature Nanotechnology*, 2014, **9**, 676–681.

17 V. O. Özçelik, J. G. Azadani, C. Yang, S. J. Koester and T. Low, *Physical Review B*, 2016, **94**, 035125.

18 C. Gong, H. Zhang, W. Wang, L. Colombo, R. M. Wallace and K. Cho, *Applied Physics Letters*, 2013, **103**, 053513.

19 M.-H. Chiu, C. Zhang, H.-W. Shiu, C.-P. Chuu, C.-H. Chen, C.-Y. S. Chang, C.-H. Chen, M.-Y. Chou, C.-K. Shih and L.-J. Li, *Nature Communications*, 2015, **6**, 7666.

20 H. M. Hill, A. F. Rigosi, K. T. Rim, G. W. Flynn and T. F. Heinz, *Nano Letters*, 2016, **16**, 4831–4837.

21 P. Rivera, J. R. Schaibley, A. M. Jones, J. S. Ross, S. Wu, G. Aivazian, P. Klement, K. Seyler, G. Clark, N. J. Ghimire, J. Yan, D. G. Mandrus, W. Yao and X. Xu, *Nature Communications*, 2015, **6**, 6242.

22 D. Kozawa, A. Carvalho, I. Verzhbitskiy, F. Giustiniano, Y. Miyauchi, S. Mouri, A. H. Castro Neto, K. Matsuda and G. Eda, *Nano Letters*, 2016, **16**, 4087–4093.

23 K. Keyshar, M. Berg, X. Zhang, R. Vajtai, G. Gupta, C. K. Chan, T. E. Beechem, P. M. Ajayan, A. D. Mohite and T. Ohta, *ACS nano*, 2017, **11**, 8223–8230.

24 A. Kutana, E. S. Penev and B. I. Yakobson, *Nanoscale*, 2014, **6**, 5820–5825.

25 X. Duan, C. Wang, Z. Fan, G. Hao, L. Kou, U. Halim, H. Li, X. Wu, Y. Wang, J. Jiang, A. Pan, Y. Huang, R. Yu and X. Duan, *Nano Letters*, 2015, **16**, 264–269.

26 J.-G. Song, G. H. Ryu, S. J. Lee, S. Sim, C. W. Lee, T. Choi, H. Jung, Y. Kim, Z. Lee, J.-M. Myoung, C. Dussarrat, C. Lansalot-Matras, J. Park, H. Choi and H. Kim, *Nature Communications*, 2015, **6**, 7817.

27 H. Li, X. Duan, X. Wu, X. Zhuang, H. Zhou, Q. Zhang, X. Zhu, W. Hu, P. Ren, P. Guo, L. Ma, X. Fan, X. Wang, J. Xu, A. Pan and X. Duan, *Journal of the American Chemical Society*, 2014, **136**, 3756–3759.

28 Q. Fu, L. Yang, W. Wang, A. Han, J. Huang, P. Du, Z. Fan, J. Zhang and B. Xiang, *Advanced Materials*, 2015, **27**, 4732–4738.

29 Y. Gong, Z. Liu, A. R. Lupini, G. Shi, J. Lin, S. Najmaei, Z. Lin, A. L. Elías, A. Berkdemir, G. You, H. Terrones, M. Terrones, R. Vajtai, S. T. Pantelides, S. J. Pennycook, J. Lou, W. Zhou and P. M. Ajayan, *Nano Letters*, 2013, **14**, 442–449.

30 S. Susarla, A. Kutana, J. A. Hachtel, V. Kochat, A. Apte, R. Vaj-

tai, J. C. Idrobo, B. I. Yakobson, C. S. Tiwary and P. M. Ajayan, *Advanced Materials*, 2017, **29**, 1702457–1702457.

31 H.-P. Komsa and A. V. Krasheninnikov, *The Journal of Physical Chemistry Letters*, 2012, **3**, 3652–3656.

32 J. Kang, S. Tongay, J. Li and J. Wu, *Journal of Applied Physics*, 2013, **113**, 143703.

33 B. Zheng, C. Ma, D. Li, J. Lan, Z. Zhang, X. Sun, W. Zheng, T. Yang, C. Zhu, G. Ouyang *et al.*, *Journal of the American Chemical Society*, 2018, **140**, 11193–11197.

34 R. Decker, Y. Wang, V. W. Brar, W. Regan, H.-Z. Tsai, Q. Wu, W. Gannett, A. Zettl and M. F. Crommie, *Nano letters*, 2011, **11**, 2291–2295.

35 J. Xue, J. Sanchez-Yamagishi, D. Bulmash, P. Jacquod, A. Deshpande, K. Watanabe, T. Taniguchi, P. Jarillo-Herrero and B. J. LeRoy, *Nature materials*, 2011, **10**, 282.

36 S. Dai, Y. Xiang and D. J. Srolovitz, *Nano letters*, 2016, **16**, 5923–5927.

37 S. Dai, Y. Xiang and D. J. Srolovitz, *Physical Review B*, 2016, **93**, 085410.

38 R. L. Anderson, *IBM Journal of Research and Development*, 1960, **4**, 283–287.

39 M.-H. Chiu, W.-H. Tseng, H.-L. Tang, Y.-H. Chang, C.-H. Chen, W.-T. Hsu, W.-H. Chang, C.-I. Wu and L.-J. Li, *Advanced Functional Materials*, 2017, **27**, 1603756–1603756.

40 J.-H. Yang and B. I. Yakobson, *Chemistry of Materials*, 2018, **30**, 1547–1555.

41 W. Tan, Z. Wei, X. Liu, J. Liu, X. Fang, D. Fang, X. Wang, D. Wang, J. Tang and X. Fan, *Scientific Reports*, 2017, **7**, 15124.

42 J. M. Sanchez, F. Ducastelle and D. Gratias, *Physica A: Statistical Mechanics and its Applications*, 1984, **128**, 334–350.

43 A. Zunger, S.-H. Wei, L. G. Ferreira and J. E. Bernard, *Physical Review Letters*, 1990, **65**, 353.

44 S.-H. Wei, L. G. Ferreira, J. E. Bernard and A. Zunger, *Physical Review B*, 1990, **42**, 9622.

45 S.-H. Su, Y.-T. Hsu, Y.-H. Chang, M.-H. Chiu, C.-L. Hsu, W.-T. Hsu, W.-H. Chang, J.-H. He and L.-J. Li, *Small*, 2014, **10**, 2589–2594.

46 L.-Y. Gan, Q. Zhang, Y.-J. Zhao, Y. Cheng and U. Schwingenschlögl, *Scientific Reports*, 2014, **4**, 6691.

47 J. P. Perdew, K. Burke and M. Ernzerhof, *Physical Review Letters*, 1996, **77**, 3865.

48 J. P. Perdew and M. Levy, *Physical Review Letters*, 1983, **51**, 1884.

49 P. Mori-Sánchez, A. J. Cohen and W. Yang, *Physical Review Letters*, 2008, **100**, 146401.

50 F. Ceballos, M. Z. Bellus, H.-Y. Chiu and H. Zhao, *Nanoscale*, 2015, **7**, 17523–17528.

51 J. Sun, A. Ruzsinszky and J. P. Perdew, *Physical Review Letters*, 2015, **115**, 036402.

52 J. Sun, R. C. Remsing, Y. Zhang, Z. Sun, A. Ruzsinszky, H. Peng, Z. Yang, A. Paul, U. Waghmare, X. Wu, M. L. Klein and J. P. Perdew, *Nature Chemistry*, 2016, **8**, 831–836.

53 V. Popescu and A. Zunger, *Physical review letters*, 2010, **104**, 236403.

54 G. Kresse and J. Furthmüller, *Computational Materials Science*, 1996, **6**, 15–50.

55 G. Kresse and J. Furthmüller, *Physical Review B*, 1996, **54**, 11169.

56 P. E. Blöchl, *Physical Review B*, 1994, **50**, 17953.

57 G. Kresse and D. Joubert, *Physical Review B*, 1999, **59**, 1758.

58 P. V. Medeiros, S. Stafström and J. Björk, *Physical Review B*, 2014, **89**, 041407.

59 P. V. Medeiros, S. S. Tsirkin, S. Stafström and J. Björk, *Physical Review B*, 2015, **91**, 041116.

60 A. Van De Walle, M. Asta and G. Ceder, *Calphad*, 2002, **26**, 539–553.

Vertical (bilayer) Heterojunction

$MA_{2(1-x)}B_{2x}$

$NA_{2(1-y)}B_{2y}$